Preprint
UCRL-JC-151535

Comparison of Model and Experimental Results for Material and Energy Flow in a Titanium Evaporation System with Deforming Interfaces

M.A. McClelland, K.W. Westerberg, T.C. Meier, D.G. Braun, K.D. Frischknecht, T.M. Anklam

This article was submitted to
Moving Boundaries 2003
Santa Fe, NM, November 4-6, 2003

U.S. Department of Energy

Lawrence
Livermore
National
Laboratory

May 12, 2003

Comparison of model and experimental results for material and energy flow in a titanium evaporation system with deforming interfaces

M. A. McClelland[1], K. W. Westerberg[1], T. C. Meier[1],
D. G. Braun[1], K. D. Frischknecht[2] & T.M. Anklam[1]
[1] *Lawrence Livermore National Laboratory, USA.*
[2] *OSRAM Opto Semiconductors Inc., USA.*

Abstract

Finite element calculations and measurements are compared for material and energy flow in a system to evaporate pure titanium. A 40 kW electron beam is used to heat the end of a 7.62 cm diameter cylindrical rod which is fed vertically through a water-cooled crucible. Vapor emanates from a liquid pool in which flow is driven strongly by buoyancy and capillary forces. At high evaporation rates, the vapor exerts strong shear and normal forces on the liquid-vapor interface. The MELT finite element code is used to calculate steady-state, axisymmetric flow and temperature fields along with liquid-solid and liquid-vapor interface locations. The influence of the vapor on the liquid top surface is treated using boundary conditions with parameters derived from Monte Carlo simulations. The upper and lower interfaces of the liquid pool are tracked using a mesh structured with rotating spines. Experimental evaporation rates are obtained from measured feed rates, and heat flow rates are determined from measured temperature rises in the cooling water. The finite element model provides a good representation of the measured evaporation rates, heat flows, and lower pool boundary locations.

1 Introduction

Electron-beam physical vapor deposition is a key step in the fabrication of metal matrix deposits for high performance aircraft components. In the process of Figure 1, a high power electron-beam is swept in vacuum over the top end of a

Ti-6V-4Al rod using a magnetic field. Metal evaporates from the top surface of the resulting liquid pool and deposits on moving ceramic fibers. The level of the pool is kept constant by advancing the rod in the vertical direction. In subsequent processing steps, the fibers are arranged and consolidated for later use in part fabrication. Goals for this process include rapid startup, high-rate deposition, composition control, and high vapor utilization.

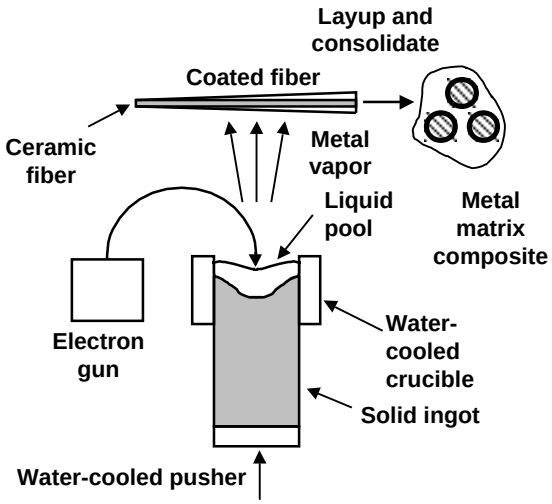

Figure 1: Electron beam deposition of vapor for the fabrication of metal matrix deposits

The behavior of this evaporation system is complex since the locations of the liquid-vapor and solid-liquid interfaces are influenced by material and energy flow (see Figure 2). The top surface of the pool deforms at the e-beam impact site from the recoil of the departing vapor. The lower boundary of the pool is a melting interface. Flow in the pool is driven strongly by density gradients (buoyancy effect), surface tension gradients (Marangoni effect), and surface shear forces generated by the expanding vapor plume.

Numerical models have been developed for metal processing and coating systems with similar features. Earlier studies involving the mesh tracking of interfaces for crystal growth, welding, and casting systems are discussed by Westerberg et al. [1]. More recently Bojarevics et al. [2] used a pseudospectral method to model an axisymmetric electromagnetic casting system with a free surface and a solidification front. Cairncross et al. [3] and Baer et al. [4] developed a finite element method for free surface flows in three-dimensions with wetting lines.

Early numerical models of e-beam evaporation systems are reviewed by Westerberg et al. [1]. More recently, we used the MELT finite element code to analyze the steady-state evaporation of aluminum from a disk confined in a

water-cooled crucible [1]. Pivoting spines were employed in the finite element method to track the moving liquid-vapor and liquid-solid interfaces along with the tri-junction. In order to test our models, material and energy flow measurements were made by McClelland et al. [5] and Westerberg et al. [6] for the evaporation of titanium alloys using the system of Figure 1. MELT finite element predictions for the evaporation rate were higher than the measured values, but showed the same linear dependence with respect to e-beam power.

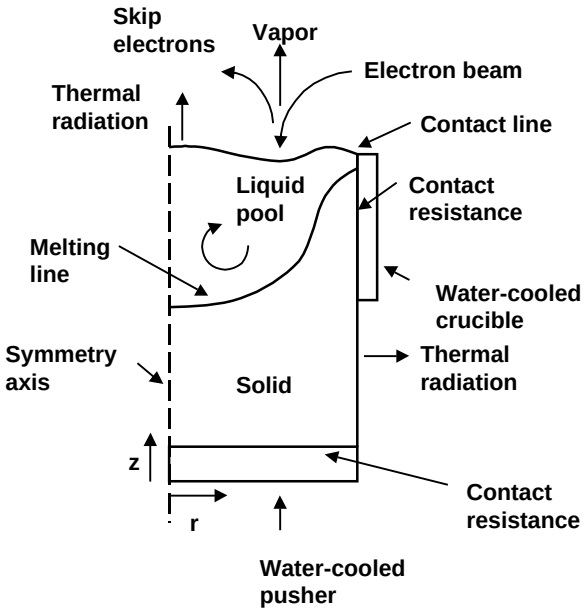

Figure 2: Finite element model for evaporation of metal from an advancing rod.

Improvements in surface evaporation models were made with Direct Simulation Monte Carlo (DSMC) methods. Fleche et al. [7] calculated the coupled vapor and liquid flow fields for the steady, axisymmetric evaporation of cerium, and they observed that the contribution of vapor shear stresses is quite important at high evaporation rates. Braun et al. [8] performed DSMC calculations for the vapor flow field and confirmed the important effects of back-scattered vapor on evaporation rates and interfacial stress.

In this work we compare model and experimental results for the titanium evaporation system of Figure 2. The finite element approach of Westerberg et al. [1] is employed with improvements to the surface evaporation model based on the DSMC results of Braun et al. [8]. The finite element results are compared with measurements made using the methods and apparatus described by McClelland et al. [5] and Westerberg et al. [6].

2 Melt evaporation model

A steady-state, two-dimensional, axisymmetric model [1, 9] is used to describe the material and energy flow in the solid ingot and liquid pool (see Figure 2). Boundary conditions derived from Monte Carlo simulations are applied at the pool surface to account for the influence of the vapor stream. The field equations for the liquid metal pool include the effects of inertia, viscosity, buoyancy, convection, and conduction. The effects of conduction are included in the solid phase. The liquid metal is treated as a Newtonian liquid with uniform bulk properties except for the density which varies linearly with temperature according to the Bousinesq approximation.

Conditions for mass, momentum, and energy are applied at the boundaries of the liquid, and solid regions. A specification is provided for the average level of the pool. At the axis of symmetry, the liquid-vapor interface is horizontal, and the contact line is fixed at the crucible lip. Since liquid circulation rates are large compared to evaporation rates, material flow rates through the top surface are taken to be negligible in modeling the flow field. Liquid does not penetrate any of the pool boundaries, and the no-slip conditions are applied at solid surfaces.

The momentum balance at the liquid-vapor interface includes the normal stress from surface tension and the tangential stress generated by thermal gradients in the surface tension (Marangoni effect). This Marangoni stress drives liquid from the hot beam area to colder regions on the top surface. The effects of back-scattered vapor are also included in the normal and shear stress components. The vapor thrust term $\pi_v = p_{vap}(T)(1+\xi_\pi)/2$ includes the factor $(1+\xi_\pi)$ to account for the increased thrust due to back-scattered vapor [10]. The expanding vapor plume also applies a shear force that drives the liquid in the same direction as the buoyancy and Marangoni effects. This surface shear force is represented by

$$\tau_V = \xi_\tau \sigma_b \frac{d\pi_V}{ds} . \qquad (1)$$

in which s is the radial surface coordinate, σ_b is a characteristic dimension of the trench, and ξ_τ is a parameter determined from Monte Carlo calculations. A similar approach was used by Fleche et al. [7].

The incident e-beam flux is taken to have a Gaussian distribution, and energy losses associated with skip electrons are taken to be a fixed fraction of the incident energy flux. At the top surface of the pool energy radiates to the cold surroundings according to a T^4 expression. The heat associated with evaporation includes latent heat and a translational contribution associated with vapor flow. The local evaporation flux is calculated using a Langmuir expression reduced by a factor $(1-\xi_n)$ to account for the influence of back-scattered vapor . The parameters ξ_n, ξ_π, and ξ_τ are determined from Monte Carlo simulations of a representative Ti evaporation process in the apparatus described below [8].

The temperature of the lower boundary of the pool is taken to be the melting point value. Thermal contact resistance between the liquid and the crucible wall is modeled with a single heat transfer coefficient. The heat loss from the solid ingot to the crucible wall has contributions from contact and thermal radiation. The thermal contact resistance between the bottom of the ingot and the pusher is also modeled with a heat transfer coefficient. In order to reduce the effort associated with meshing, the finite element domain is kept at a length shorter than the ingot. The lower portion of the ingot is modeled as a cooling fin, since the temperature varies primarily in the axial direction. An effective heat transfer coefficient at the lower boundary of the finite element domain accounts for the thermal behavior in the lower section of the ingot.

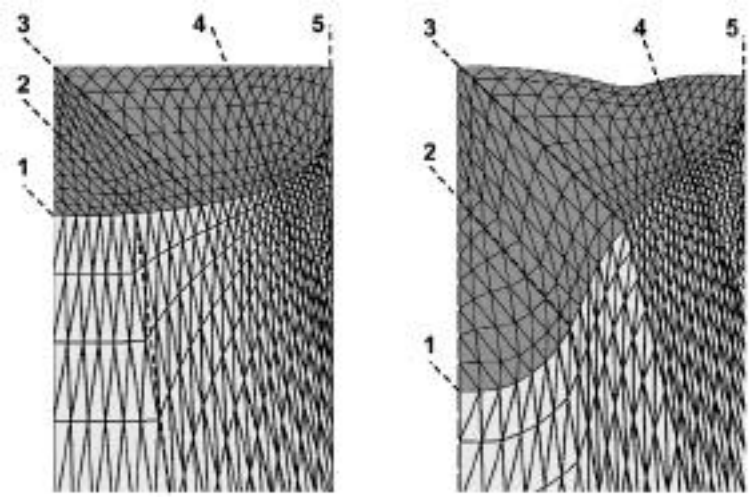

Figure 3: Finite element mesh deforms using pivoting and stretching spines.

The field and boundary equations are discretized using a Galerkin finite element method. We use a mesh with two sets of rotating spines as is illustrated in Figure 3. Each spine in the first set (nos. 1-3) begins at a common anchor point above and to the left of the pool. These spines enter the liquid along the axis of symmetry, bend at the solid-liquid interface, and proceed to base points along the lower and right boundaries of the solid region. The first and last spines (nos. 1 and 3) in this set pass through the axis of symmetry at the junctions with solid-liquid and liquid-vapor interfaces, respectively. Each spine in the second set (nos. 4, 5) begins at an anchor point above the top of the ingot. They pass through the liquid-vapor interface, bend at the solid-liquid interface, and end at anchor points along the outside radius of the ingot. The last spine (no. 5) in this set is vertical and passes through the contact line and liquid-solid

interface at the crucible wall. As in the earlier studies, the interfacial mesh points move with the interfaces while the interior points move along the spines.

This mesh strategy helps with the tracking of nearly vertical liquid boundaries encountered in deep pools. The use of vertical spines leads to excessive mesh deformation. The diagonal rotating spines of this study provide for less mesh deformation since spines are more orthogonal to the solid-liquid interface. The baseline cases in this study had 21,655 unknowns.

As in earlier studies, the MELT computer code is used to solve the locations of the two interfaces simultaneously with the flow and temperature fields using the Newton-Raphson method. All results in this work are steady-state, but some were found by integrating from one steady-state point to another point using the false-transient method [11]. The backward Euler method was used with large time steps and error tolerances to damp strong transients and progress rapidly through the parameter space to the point of interest. This approach was particularly effective for traversing regions of the parameter space for which steady-state solutions were not available using traditional parameter continuation methods.

3 Experimental

Evaporation experiments with titanium were conducted in the Evaporation Test Facility (ETF) at Lawrence Livermore National Laboratory. The ETF chamber has a bottom-fed crucible in which a rod of the evaporation metal is advanced through a water-cooled crucible with a water-cooled pusher. A side-mounted 50 kW electron-beam gun provides the energy for evaporation and was operated at 33.3 kV in these experiments. Magnets were used to sweep the electron beam in a ring pattern on the top of a 0.0762 m diameter feed rod of commercially pure Ti. The beam had a 0.6 cm spot size and was swept at a rate of 3 kHz. A vapor enclosure consisting of water-cooled copper panels captures the vapor above the crucible and has openings to accommodate the electron beam and camera views. All water-cooling circuits in the chamber have thermocouples and flow meters, allowing heat flows to be computed using standard calorimetric methods.

Two pin-hole cameras with argon gas bleed are mounted inside the vacuum chamber to view the vapor source. The high angle view of the vapor source is used to position and monitor the beam on the ingot top, and the low angle view is used to measure the liquid pool height.

The pool level is determined by applying an edge detection routine to images captured with the low angle camera. In order to provide a well-defined edge, the liquid pool surface was run at a relatively high level with the top surface bulging above the crucible lip. This bulge can be created with a minimum of overflow due to the relatively high surface tension and low density of titanium. The liquid pool level is maintained at its set-point value by adjusting the feed rate using a feedback control system with the e-beam power constant. The evaporation rate is determined from the consumption of feed material with a correction for metal overflow onto the crucible.

4 Comparison of results

4.1 Conditions

Evaporation measurements were made in five runs with titanium. In these runs, the e-beam power was varied from 38 to 46 kW. Each run was divided into periods in which conditions were held constant. Approximately 2.5 cm (0.5 kg) of metal was fed in each period. At the end of each the e-beam was quickly shut off to preserve the shape of the solid-liquid interface. A post-run sectioning revealed the shape of the solid-liquid interface.

Table 1 Properties and parameters for evaporation of titanium metal

Liquid properties	Value	Units	Vapor , solid properties	Value	Units
Melting pt.	1667	°C	Vap. pressure	$p_1 \exp(E/RT)$	N/m^2
Molecular wt.	0.0479	kg/gmol	p_1	2.32×10^{11}	N/m^2
			E	-4.35×10^5	J/gmol
Density	4130	kg/m^3	Heat vap.	9.09×10^6	J/kg
Viscosity	3.20×10^{-3}	kg/m-s			
Vol. expan.	5.57×10^{-5}	K^{-1}	Vapor backscatter		
Therm. cond.	31.0	W/m-K	Mass, ξ_n	0.200	
Heat capacity	8.84×10^2	J/kg-K	Nrm. thrust, ξ_π	0.123	
Surface tens.	1.65	N/m	Vapor shear, ξ_τ	0.0288	
Temp. deriv.	-2.40×10^{-4}	N/m-K	Beam spot		
Therm. emis.	a_0+a_1T		rad., σ_b	0.003	m
a_0	0.1810				
a_1	2.53×10^{-5}	K^{-1}	Solid prop.		
Skip fraction	0.22		Therm. cond.	31.0	W/m-K
			Therm. emis.	0.4	
Therm. Tr., ζ	1.0-1.092				

4.2 Properties and model parameters

For the modeling of these experiments with the MELT code, most physical properties are assigned their melting points values for the respective phases (see Table 1). One exception is the viscosity which is a factor of 15 higher to accommodate the strong convection encountered in this study. The use of this high viscosity provides converged steady-state solutions with good mesh resolution. Even with this increased viscosity the flows are still quite intense with Reynolds and Peclet numbers having magnitudes of approximately 1000. In an attempt to compensate for the reduced thermal transport resulting from the artificially increased viscosity, the convection and conduction terms in the energy equation are increased in some cases by a factor ζ. This factor allows the thermal transport to be increased without the need for finer meshes, time-

dependent simulations, or turbulent flow models. The parameters ξ_n, ξ_π, and ξ_τ associated with liquid-vapor interactions were determined from Monte Carlo results [8, 9]. The back scattering of vapor results in 20% of the vapor returning to the surface and a 12% increase in vapor thrust. The influence of the vapor shear parameter ξ_τ is discussed below.

Except for the e-beam footprint, the geometric parameters from the final period of Run No. 3 were taken to be representative for the experiments of this study. The e-beam ring diameter and spot size were 4.8 and 0.48 cm for Run No. 3 and 4.7 and 0.6 cm for all other cases. As a result of operating the pool at a high level there was metal overflow onto the crucible by the end of each run.

The heat transfer coefficient for the liquid in contact with the crucible is 7000 W/m^2-K and for the pusher is 100 W/m^2-K. These values are in the range of values reported for liquid and solid metals in contact with cold surfaces [12]. The heat transfer coefficient for the solid contact with the crucible decreases linearly with temperature from the liquid value at the melting point to zero at 300 °C below the melting point. The cooling fin model for the lower section of the ingot also gives an effective heat transfer coefficient of 83 W/m^2-K for the lower surface of the shortened model domain. As the length of the model domain increases, the increase in the axial conduction resistance is balanced by the increase in ingot area at the outside radius and an associated increase in heat loss by thermal radiation.

4.3 Pool boundary location and local heat flows

For the last period of Run No. 3, the predicted stream function and temperature contours, interface locations, and heat flows are show in Figure 4 along with the measure heat flows and frozen solid-liquid interface. The MELT model includes the effect of vapor shear and no artificial increase in thermal transport (τ_v, ς=1). The predicted and measured depths of the pool agree to within 6% and both the model and measured pool boundaries show an inflection point. Two counter-rotating cells are present in which the surface liquid flows from the hot beam area towards the cold wall and the cooler region near the symmetry axis. The buoyancy, Marangoni, and vapor shear forces all have the same sign and all contribute significantly to the flow pattern.

The heat flows predicted by the MELT model agree with the measured values (see Figure 4). The model flow and temperature fields are well resolved since the incident e-beam power differs from the total heat removed by 0.7%. These same quantities agree to within 0.5% for the experiment. Both the model and measure heat flows indicate approximately 40% of the energy is lost from the top of the ingot. Only 8% of the energy is used for evaporation of the titanium.

4.4 Evaporation rates and enclosure heat flows

Measured bulk evaporation rates and enclosure heat flows are plotted versus e-beam power in Figures 5 and 6. The enclosure heat flow is the sum of the skip, evaporative, and radiative energy emanating from the top surface of the melt. In each experimental run the sensitivity of evaporation rate to e-beam power is nearly constant. This sensitivity is also constant from one run to the next. However, there seems to be offsets between measurements taken during different runs, suggesting some type of systematic variation. This same behavior is observed for the enclosure heat flows. Although the cause of the run-to-run variations is not known, it is probably the result of some variation in the e-beam power delivery which has the strongest influence on melt behavior.

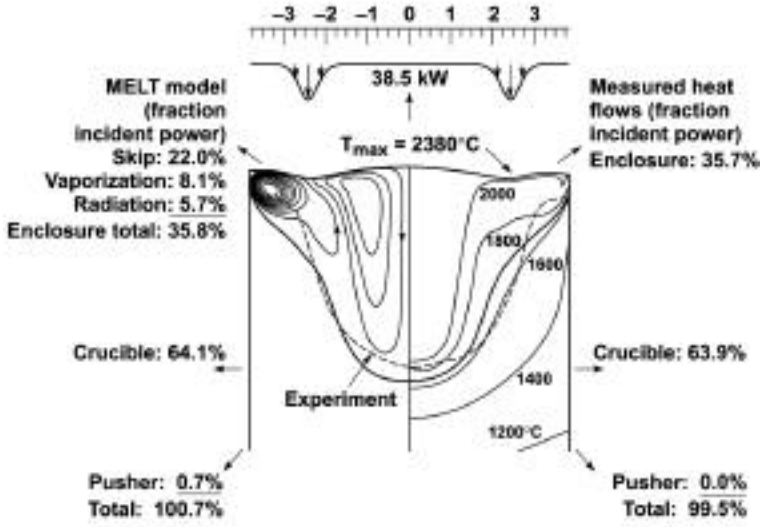

Figure 4: Comparison of model (τ_v, ς=1.0) and measured heat flows and pool boundaries for Ti Run No. 3, final run period.

MELT model predictions for evaporation rate and enclosure heat flow are shown for three cases in Figures 5 and 6. For the case of excluded vapor shear and baseline thermal transport (τ_v=0, ς=1), evaporation rates and enclosure heat flows are approximately 50% higher than measured values. These are the results reported in an earlier study [6]. For the same case with vapor shear included (τ_v, ς=1) evaporation and enclosure heat flows are in good agreement with measured values. The presence of vapor shear greatly increases the circulation rates and decreases the hot zone temperature and the evaporation rates. The inclusion of this effect greatly improves the model representation of the measurements. For a case in which the thermal transport is further increased artificially (τ_v, ς=1.092) the representation of the data is even better. This

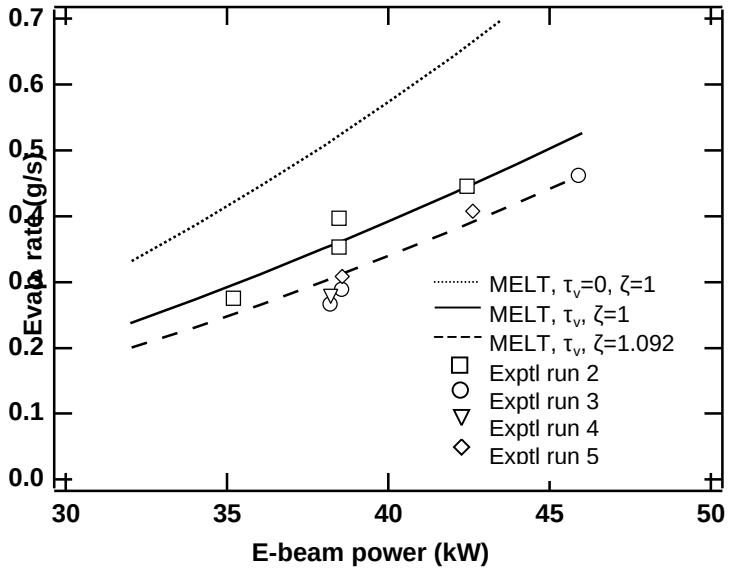

Figure 5: Comparison of model and measured bulk evaporation rates for Ti.

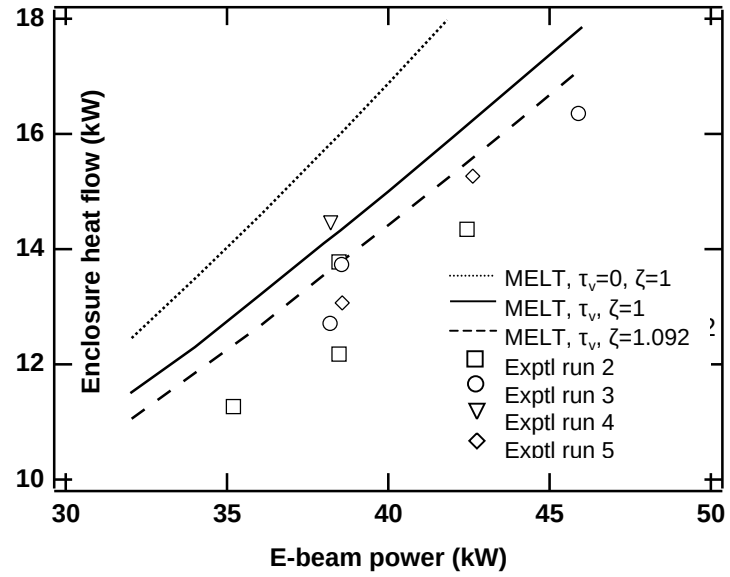

Figure 6: Comparison of model and measured enclosure heat flows for Ti.

increase compensates to some extent for the reduced thermal convection resulting from the artificially high viscosity (15X) needed to achieve numerical stability.

5 Conclusions

A MELT finite element model is applied to experimental results for the electron beam evaporation of titanium. The finite element method incorporates diagonal spines to track solid-liquid and liquid-vapor interfaces of deep pools. The model uses boundary conditions at the liquid surface to account for vapor-liquid interactions, including the shear force imparted by the expanding vapor on the liquid surface. The parameters in these boundary conditions were calculated using Monte Carlo simulations. In the experiments, bulk evaporation rates were measured by feed consumption, and heat flows were measured by calorimetry. The measurements show a nearly constant dependence on e-beam power despite run-to-run offsets in the measurement curves. The comparison of model and measured results shows that the inclusion of vapor shear in the model leads to a good representation of evaporation rates, heat flows, and liquid-solid interface locations.

6 Acknowledgments

Rich Palmer developed, operated, and maintained the electron gun as well as implemented the feeder controller and data acquisition systems in ETF. Paul Gronner operated and maintained the vacuum and mechanical systems in ETF. This work was partially support by DARPA through the vapor phase manufacturing initiative (administered by Steve Wax). This work was performed under the auspices of the U.S. Department of Energy by Lawrence Livermore National Laboratory under Contract W-7405-Eng-48.

References

[1] Westerberg, K. W., McClelland, M. A. & Finlayson, B. A., Finite element analysis of flow, heat transfer, and free interfaces in an electron-beam vaporization system for metals, *Int. J. Numer. Meth. Fluids*, **26**, pp. 637-655, 1998.

[2] Bojarevics, V., Pericleous, K. & Cross, M., Modeling the dynamics of magnetic semilevitation melting, *Metall. Trans. B.*, **31B**, pp. 179-189, 2000.

[3] Cairncross, R. A., Schunk, P. R., Baer, T. A., Rao, R. R. & Sackinger, P. A., A finite element method for free surface flows of incompressible fluids in three dimensions. Part 1. Boundary fitted mesh motion, *Int. J. Numer. Meth. Fluids*, **33**, pp. 375-403, 2000.

[4] Baer, T. A., Cairncross, R. A., Schunk, P. R., Rao, R. R. & Sackinger, P. A., A finite element method for free surface flows of incompressible fluids in three dimensions. Part II. Dynamics wetting lines, *Int. J. Numer. Meth. Fluids*, **33**, pp. 405-427, 2000.

[5] McClelland, M. A., Westerberg, K. W., Meier, T. C., Braun, D. G., Berzins, L. V., Anklam, T. M. & Storer, J., Experimental and numerical study of the e-beam evaporation of titanium, *Proceedings of the Electron Beam Melting and Refining State of the Art 1996*, ed. R. Bakish, Bakish Materials Corporation, Englewood, NJ, 1996.

[6] Westerberg, K. W., Meier, T. C., McClelland, M. A., Braun, D. G., Berzins, L. V. & Anklam, T. M., Analysis of the e-beam evaporation of titanium and Ti-6Al-4V, *Proceedings of the Electron Beam Melting and Refining State of the Art 1997*, ed. R. Bakish, Bakish Materials Corporation, Englewood, NJ, pp. 208-221, 1997.

[7] Fleche, J. L., Saunois, P. & Guilbaud, D., Effect of the backscattered vapor pressure on the temperature field of a metal heated by an electron beam, *Proceedings of the 21st International Symposium on Rarefied Gas Dynamics*, pp. 1-8, 1998.

[8] Braun, D. G., Anklam, T. M., Berzins, L. V., Blackfield, D. T., McClelland, M. A., Meier, T. C., Boyd, I. & Balakrishnan, J., Simulation of an EBPVD titanium vapor plume and comparison to experiment, *Proceedings of the Electron Beam Melting and Refining State of the Art 1998*, ed. R. Bakish, Bakish Materials Corporation, Englewood, NJ, 1998.

[9] McClelland, M. A., Westerberg, K. W., Meier, T. C., Braun, D. G., Frischknecht, K. D. & Anklam, T. M., Comparison of finite element and experimental results for material and energy flow in a titanium evaporation system, in preparation.

[10] Tran-Cong, T. & Bird, G. A., One-dimensional outgassing problem, *Phys. Fluids*, **21**, pp. 327-333, 1978.

[11] Gresho, P. M., Lee, R. L. & Sani, R. L., On the time-dependent solution of the incompressible Navier-Stokes equations in two and three dimensions. *Recent Advances in Numerical Methods in Fluids*, eds., C. Taylor & K. Morgan., Pineridge Press, Ltd.: Swansea, UK, pp. 27-79, 1980.

[12] Ransing, R. S., Zheng, Y. & Lewis, R. W., Potential application of intelligent preprocessing in the numerical simulation of castings, *Proceedings of the Numerical Methods in Thermal Problems*, ed. R. W. Lewis, Pineridge Press, Swansea, pp. 361-375, 1993.